RESEARCH ARTICLE

NANO · MICRO small
www.small-journal.com

Graphene via Microwave Expansion of Graphite Followed by Cryo-Quenching and its Application in Electrostatic Droplet Switching

Sumit Chahal, Trisha Sahay, Zhixuan Li, Raju Kumar Sharma, Ekta Kumari, Arkamita Bandyopadhyay, Puja Kumari, Soumya Jyoti Ray, Ajayan Vinu, and Prashant Kumar**

Monoelemental atomic sheets (Xenes) and other 2D materials offer record electronic mobility, high thermal conductivity, excellent Young's moduli, optical transparency, and flexural capability, revolutionizing ultrasensitive devices and enhancing performance. The ideal synthesis of these quantum materials should be facile, fast, scalable, reproducible, and green. Microwave expansion followed by cryoquenching (MECQ) leverages thermal stress in graphite to produce high-purity graphene within minutes. MECQ synthesis of graphene is reported at 640 and 800 W for 10 min, followed by liquid nitrogen quenching for 5 and 90 min of sonication. Microscopic and spectroscopic analyses confirmed the chemical identity and phase purity of monolayers and few-layered graphene sheets (200–12 µm). Higher microwave power yields thinner layers with enhanced purity. Molecular dynamics simulations and DFT calculations support the exfoliation under these conditions. Electrostatic droplet switching is demonstrated using MECQ-synthesized graphene, observing electrorolling of a mercury droplet on a BN/graphene interface at voltages above 20 V. This technique can inspire the synthesis of other 2D materials with high purity and enable new applications.

1. Introduction

Atom-thin materials including Xenes (a generic name for mono elemental atomic sheets e.g., graphene,[1–3] phosphorene,[4,5] borophene,[6–12] silicene,[13] germanene,[14] 2D gold,[15] berylline,[16] molybdenene,[17] etc.), 2D metal oxides,[18–20] 2D nitrides,[21] MXenes,[22] etc. have grabbed extreme attention in recent times due to their unique physical and chemical properties. Common traits are high electronic mobility, high Youngs moduli, high thermal conductivity etc.[3,23] They exhibit great potential for commercial applications. Graphene in particular has been established as wonder material for the 21st century as it has been demonstrated to have broad applications including those in electronics,[24] photonics/optoelectronics,[25–27] spintronics,[28] laser shield,[29] molecular sensing,[30,31] manipulation of single

S. Chahal, T. Sahay, E. Kumari, P. Kumari, S. Jyoti Ray, P. Kumar
Department of Physics
Indian Institute of Technology Patna
Bihta Campus, Patna 801106, India
E-mail: Prashant.Kumar@newcastle.edu.au

S. Chahal
Indian Institute of Technology Hyderabad
Kandi, Hyderabad 502284, India

Z. Li, A. Vinu, P. Kumar
Global Innovative Centre for Advanced Nanomaterials (GICAN)
University of Newcastle
Callaghan 2308, Australia
E-mail: Ajayan.Vinu@newcastle.edu.au

R. K. Sharma
Department of Mechanical Engineering
Government Engineering College Sheohar
Chhatauna Bisunpur, Block- Piprahi, Sheohar, Bihar 843329, India

E. Kumari
Department of Metallurgical and Materials Engineering
Indian Institute of Technology Patna
Bihta Campus
Patna 801106, India

A. Bandyopadhyay
Institut für Physik, Theoretische Physik
Martin-Luther-Universität Halle-Wittenber
06120 Halle, Germany

The ORCID identification number(s) for the author(s) of this article can be found under https://doi.org/10.1002/smll.202404337

DOI: 10.1002/smll.202404337

photon emission,[32,33] anti-oxidation,[34] energy storage,[35,36] reversible storage of hydrogen/halogen.[37,38] Material behavior of graphene can be manipulated at will via 3D straining,[39] doping,[40] and 2D-2D hybridization.[41,42]

While bottom-up synthetic approaches result in better crystalline quality, they are costly and non-scalable.[3,23,43,44] On the other hand, top-down synthesis of these advanced materials in liquid phase via solvothermal or modified Hummer's methods is time-consuming and yields poor crystal quality due to surface oxygenation.[45,46] Laser synthesis of graphene sheets and nanoribbons in dimethylformamide offers better quality.[47–51] Other methods include cryoexfoliation,[52–56] microwave-driven exfoliation,[57–59] heating and cryoquenching,[60] and combining cryoquenching with microwave techniques.[61] Given the increasing application of these materials in everyday appliances, there is a pressing need to develop economic, scalable, and rapid synthetic protocols. Therefore, we are at a crossroads, anticipating the invention of innovative synthetic approaches in the near future.

Microswitches have garnered significant attention in MEMS technology, particularly due to their applications in IC chips.[62] They offer a high OFF/ON resistance ratio, low loss, low power consumption, linear response, and robust performance under various operating conditions such as voltage, current, temperature, pressure, and radiation. These attributes make them highly suitable for applications including field-programmable gate arrays. However, traditional beam-type microswitches face limitations such as high solid–solid contact resistance and dimensional constraints. To address these limitations, liquid metal-based electrostatic actuators have been developed. These actuators overcome some of the challenges of beam-type actuators but require high operating voltages of around 100–150 V.[63,64] Liquid metal-based MEMS microswitches must possess linear response, low contact resistance, minimal surface wear and degradation, high stability, bi-stability without a latching mechanism, electrostatic actuation, and ease of fabrication and integration.[65] Material quality, including minimal surface functionalization and defects, along with the ease of synthesis and fabrication/integration of devices, are crucial considerations for electrostatic droplet switches. Graphene, with a dielectric constant of ≈6,[66] and boron nitride (BN), with dielectric constants of 7 (in-plane) and 3.7 (out-of-plane),[67] can be heterolayered to form active electrodes for electro-rolling, an essential feature for electrostatic droplet switches. Therefore, the development of electronic-grade graphene and BN is vital for advancing electrostatic droplet switch applications.

Having the above-mentioned urgency in mind to develop novel synthetic strategies for 2D materials, exotic thermal stress caused by microwave expansion followed by cryoquenching (MECQ) has been exploited for the first time to accomplish facile synthesis of graphene and the discovery is reported in this article. As graphite is an excellent microwave absorber, microwave heating at the focal spot can generate significant expansion owing to set of exotic thermodynamic and electric field conditions. Expanded stack of atomic sheets of carbon in graphite upon cryoquenching by pouring liquid nitrogen (77 K) is supposed to spontaneously burst into exfoliation, as a materials inherent response to thermal stress created therein. Cryoquenching can thus result in facile synthesis of graphene. Microwave power was fixed at 800 and 640 W respectively in two different synthesis experiments and the effect of variation of microwave power on quality of graphene so produced has been studied. The synthesized materials have been characterized by host of microscopic techniques such as scanning electron (SEM), atomic force microscopy (AFM), transmission electron microscopy (TEM) and spectroscopic techniques such as UV–vis, Raman, and X-ray photoelectron spectroscopy (XPS). Born Oppenheimer molecular dynamics simulation of microwave expansion process and DFT calculation of nitrogen intercalated bilayer graphene has been carried out to understand the process better. Synthesized graphene was explored for electrowetting and also implemented for graphene/BN based electrostatic droplet switching application using novel materials synthesis developed in this research.

2. Results and Discussion

When graphite powder was exposed to microwave irradiation, it became red hot very fast within few seconds (**Figure 1a**). Microwave power absorption by a material is determined by its dielectric and magnetic properties:[41] $\boldsymbol{P} = 2\pi \boldsymbol{f}(\varepsilon_0\, \varepsilon'\, E^2 + \mu_0 \mu' H^2)$. Since graphite is intrinsically non-magnetic, second term can be ignored and thus, $\boldsymbol{P} = 2\pi \boldsymbol{f} \varepsilon_0 \varepsilon' \mathrm{E}^2$. Absorbed microwave power by graphite will primarily be dissipated through heating it and thus raising the temperature of graphite. $\boldsymbol{Pt} = \boldsymbol{x} k_B \boldsymbol{T}$. Where, k_B is Boltzmann constant and T represents temperature attained after microwave heating and **x** is materials dependent constant responsible for conversion of electromagnetic energy to thermal energy. This temperature manifests in terms of velocity of sheets comprising of atoms. Higher temperature means higher sheet velocity. At equilibrium distance ($\mathbf{r_{min}}$) between the layers, Lennard Jones potential σ_{LJ} is minimum. $\sigma_{LJ} = 4\epsilon(\frac{\sigma}{r^{12}} - \frac{\sigma}{r^{6}})$. The potential energy curve becomes flattish due to the relatively faster decrease of the repulsive forces compared to the attractive forces, leading to an anharmonic potential. Consequently, at higher temperature (vibrational energy), $\mathbf{r_{min}}$ keep on increasing resulting in thermal expansion. It should be noted that the linear expansion along the c-axis dominates in isobaric volumetric thermal expansion coefficient of graphite. Therefore, generated heat due to microwave absorption is predominantly utilized in the expansion of graphite in out-of-plane direction.[68] MECQ process can be depicted as the sequence of events as illustrated in Figure 1a.

Essentially, van der Waals interactions between atomic layers in graphite can be assumed (modeled for the purpose of understanding and simplicity) as if they were tiny springs with spring constant **k** defining the interaction strength. Out-of-plane expansion and contraction of graphite thus can be understood in terms of expansion and contraction of spring made up of thin filaments (extremely sensitive to heat) under heating and cooling. Choice of microwave heating (640 and 800 W) is very unique for graphite as it is an excellent microwave absorber. Microwave absorption and conversion of electromagnetic energy to heat energy involves a non-linear process under a set of exotic thermodynamic conditions and visible microwave generated plasma has been observed in the present case of microwave irradiation of the graphite powder. When microwave expanded (extreme expansion in c-direction) graphite is exposed to liquid nitrogen, the graphite material experiences a thermal shock (from >1300 to 77 K within a second).[69] Expanded graphite contracts extremely fast with

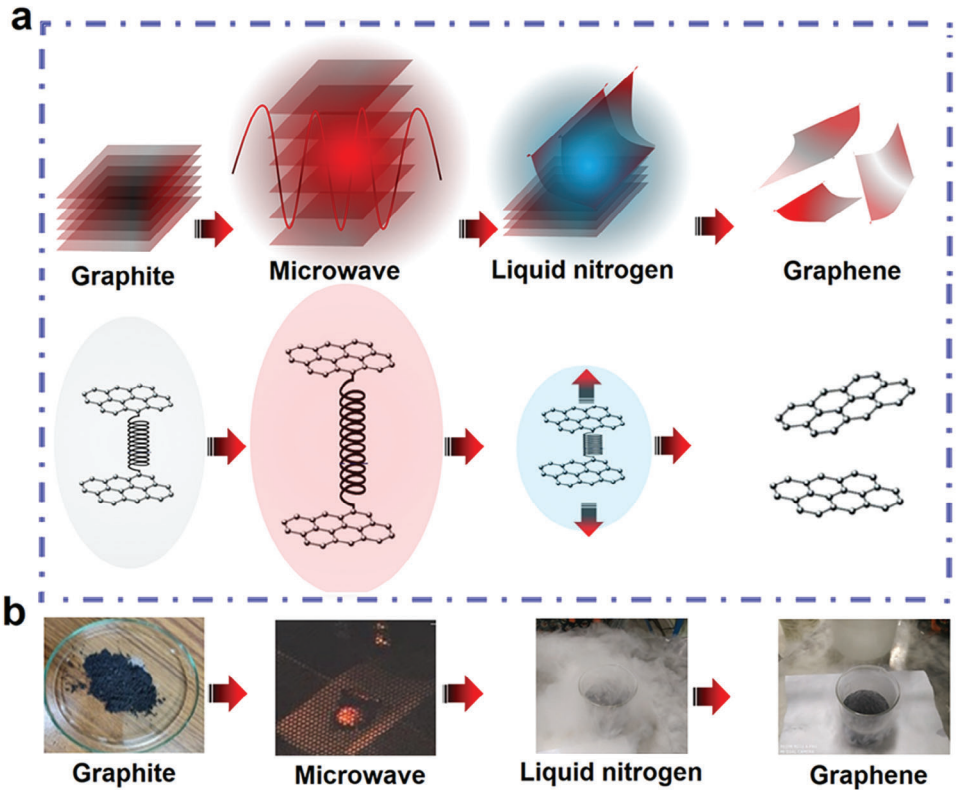

Figure 1. a) Schematic diagram showing MECQ synthesis of graphene, b) Camera image of experiment at various stages of synthesis.

extremely high velocity and atomic layers breaches the equilibrium distance between them i.e. 3.3 Å. The material cannot sustain such compressive stress for long and there is a spontaneous expansion of graphite crystal leading to exfoliation of graphite. No harsh chemical reagent is used in the exfoliation process, and thus it is completely green synthetic strategy. Figure 1b complements this with camera images capturing the various stages of the MECQ process. Scalable synthesis of graphene was achieved, as showcased in Figure S1 (Supporting Information). SEM image of typical multilayer graphene is shown in Figure S2 (Supporting Information). Finally, subsequent ultrasonication (90 min) in IPA solvent facilitates even better exfoliation of graphite into graphene.

The morphological characteristics of the synthesized graphene were examined using SEM and AFM techniques. The SEM images (**Figure** 2a,b) vividly illustrate the layered structure of exfoliated graphene synthesized at microwave powers of 640 and 800 W, respectively, showcasing its remarkable thinness and transparency under a 10 kV electron beam. We could observe thick stacks of multilayered sheets (red rectangle region in Figure 2a) for 640 W sample. Higher microwave power (800 W) sample however resulted in thinner sheets (yellow rectangle region) and folds (light green rectangle region). In general, flat atomically thin monolayers are often transparent and multilayers of the same 2D material are less in optical transparency. Electronic transparency has to do with electrical conductivity. Samples with less surface defects and oxygen functionalities are electronically opaque. Subsequent AFM analysis (Figure 2c–f) further corroborates these findings, providing quantitative insights into the thickness of the graphene. The AFM results indicate that the thickness of the synthesized graphene is ≈1.5 nm, corresponding to ≈4 layers. Statistical analysis of AFM images (Figure 2g–j) reveals that the microwave power exerts a notable influence on both the lateral dimensions and the number of layers of graphene. Specifically, higher microwave power settings result in a reduction in the number of graphene layers (peak ≈7–9 for 640 W to peak ≈4–6 for 800 W) and an increase in lateral dimensions (peak ≈2 µm for 640 W to peak ≈3 µm for 800 W). Microwave frequency used in domestic ovens are fixed at $\mathbf{f} = 2.45$ GHz.

We experimentally observed that 640 W (i.e. 80 % maximum reactor power) gives rise to relatively thicker graphene sheets (maximum being 7–9 layers) with smaller lateral dimensions (2–3 µm). In contrast, 800 W (i.e. 100 % power) gives rise to thinner (maximum being 4–6 layers) sheets with larger (3–4 µm) lateral dimensions. Increase of 25 % in microwave power will lead to higher thermal gradient (linear relation with power) and hence thermal shock will be more severe, when cryo-quenching is subsequently carried out on microwave expanded graphite samples.

TEM was employed to investigate the crystallinity and atomic structure of the synthesized graphene. The typical TEM images (**Figure** 3a,g) depict multi-layered structure of the graphene synthesized at microwave powers of 640 W and 800 W, respectively. Notably, the graphene synthesized at 800 W exhibits fewer layers and larger lateral dimensions compared to that synthesized at 640 W. HRTEM further elucidates the atomic-scale structure of the synthesized graphene. In the HRTEM image (Figure 3b,h), the in-plane distance between atoms displays a stretched pattern rather than a perfect hexagonal arrangement.

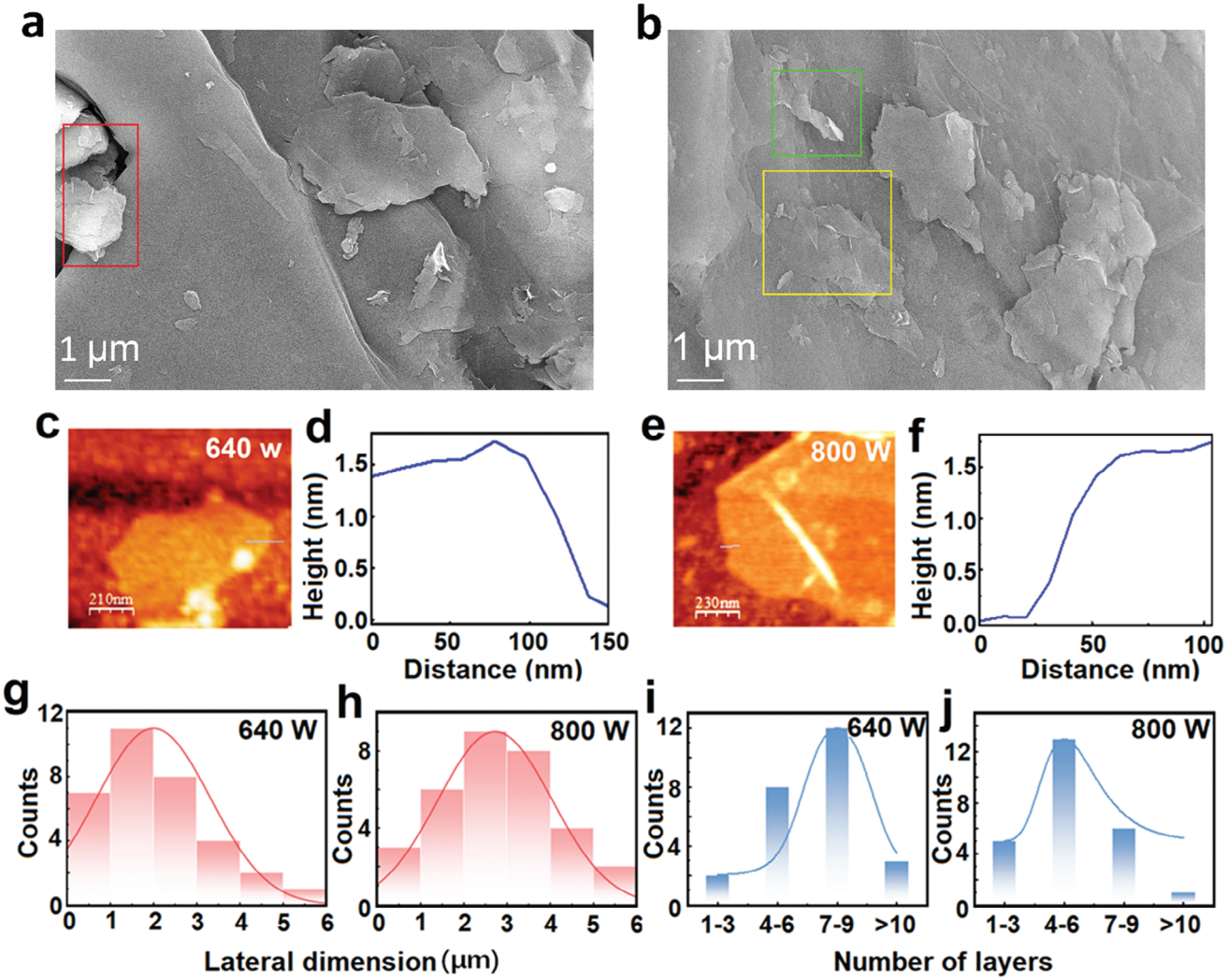

Figure 2. SEM images of graphene sheets obtained after 1 h of sonication of cryoquenched graphite sample for MW expansion carried out at microwave power a) 640 W and b) 800 W. Corresponding AFM images and line profiles for graphene samples when c,d) 640 W and, e,f) 800 W was used. Lateral dimension distribution of graphene sheets obtained at g) 640 W and h) 800 W. Number of layer distribution histograms plotted for graphene sheets obtained at i) 640 W and j) 800 W.

This observation implies the existence of strain-induced distortions in the graphene lattice, resulting in deviations from ideal hexagonal symmetry. Zoomed-in regions (1 and 2) of the HRTEM image (Figure 3c,e,i,k) and the measured atom distances (Figure 3d,f,j,i) offer detailed insights into the atomic-scale features of the graphene lattice. The stretched pattern of atomic arrangements indicates the presence of strain effects that disrupt the regular hexagonal structure, further corroborating the presence of lattice distortions induced by residual strain caused by thermal stress during microwave processing. Inter-atomic distances between consecutive atoms in graphene theoretically is ≈1.4 Å. Depending on the noises generated during HRTEM measurement (at low vacuum conditions for example), contrast of the image is degraded. For the same level of image contrast in same set of imaging, factors responsible for variation in inter-atomic distances are: a) number of layers in the atomic sheets (Larger number of layers have better coupling and they come close to each other, lateral distances increases between atoms in sheets; compared to monolayers), b) lattice defects (such as vacancies/vacancy clusters, Stone Wales defects etc.), c) oxygen functionalities (epoxy for example), (d) local residual strain in the system, e) moire potential acting (especially for bilayer/multilayer stacks).

When driving thermal stress is less, the undergoing cooling process adopts equilibrium pathway. However, when the material is undergone through thermal shock ≈1400 K within fraction of second, material experiences non-equilibrium phenomenon causing enormous thermal stress gradient even in-plane giving rise to ripples, local defects etc. (as has been observed in HRTEM imaging (Figure 3i,k), and evident from atomistic line profile).

Raman spectroscopy indicated the presence of defects and disorder within the graphene lattice. Analysis of the Raman spectra (**Figure** 4a,d) obtained from graphene samples synthesized at two different microwave power settings reveals notable

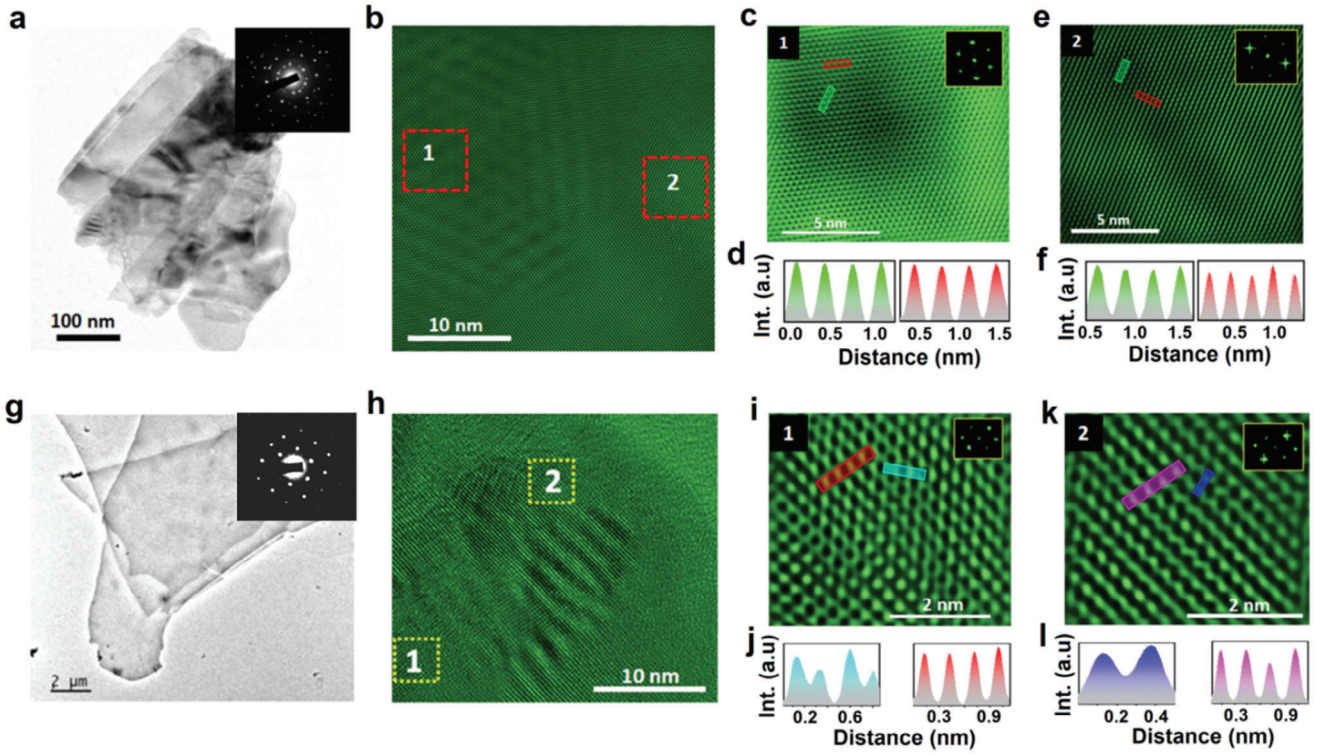

Figure 3. TEM images of graphene sheets obtained after 1 h of sonication of cryoquenched graphite sample for MW expansion carried out at microwave power a) 640 W and g) 800 W. HRTEM images and atomically resolved zoomed-in images for samples obtained at b,c,e) 640 W and h, I,k) 800 W. Atomistic line profiles along two directions as marked in images are shown in (d,f,j,l) corresponding to zoomed-in images (c,e,i,k) respectively.

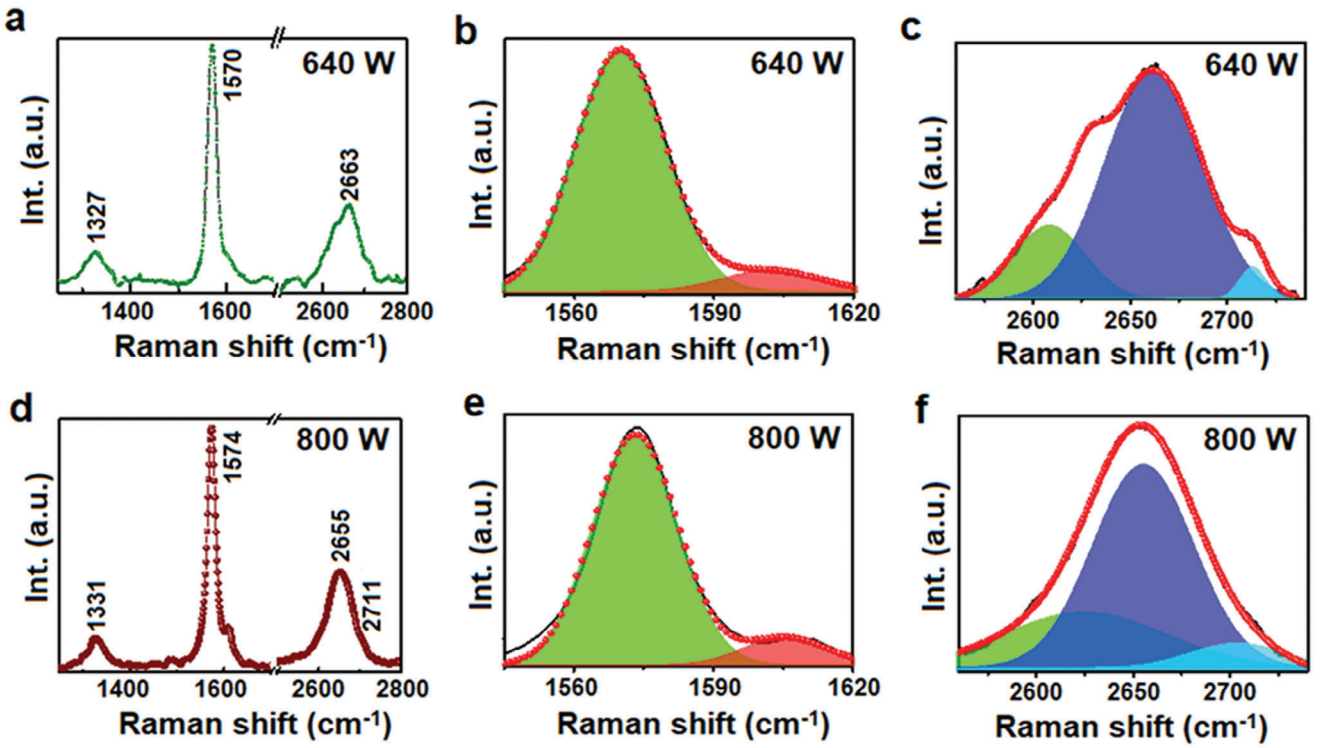

Figure 4. Typical Raman spectra for samples obtained at MW power a) 640 W and d) 800 W. Corresponding deconvoluted G-peak and 2D peaks for b,c) 640 W and e,f) 800 W samples.

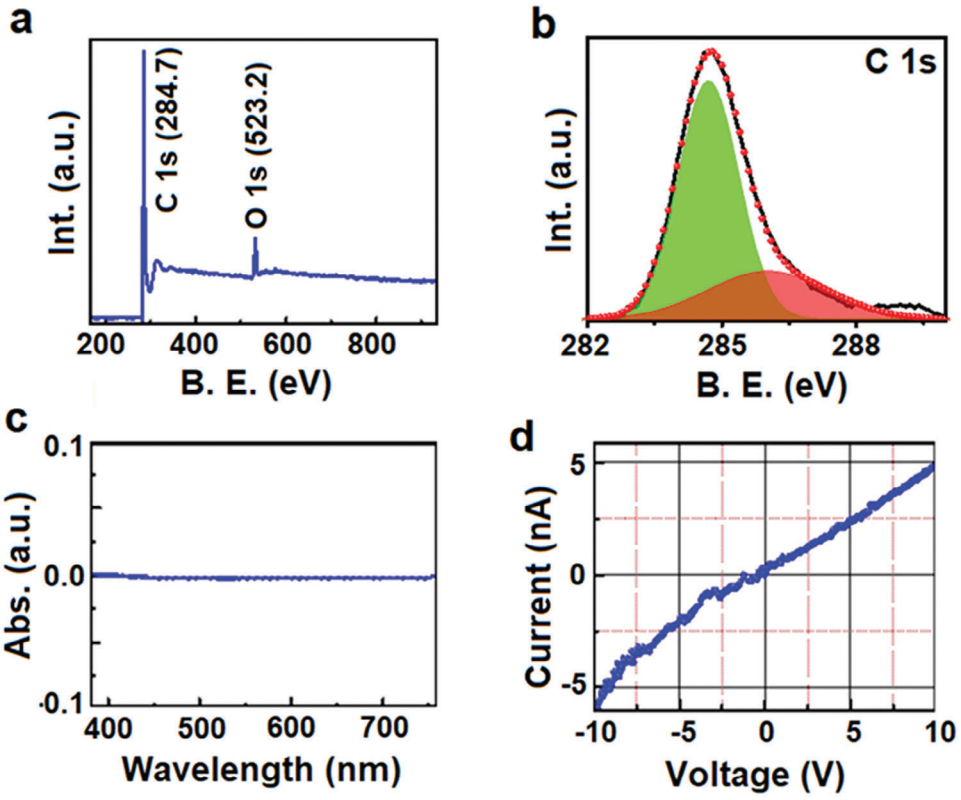

Figure 5. a) Survey XPS spectrum and b) deconvoluted C 1s resolved peak. c) UV–vis spectrum of typical obtained dispersion containing few-layered graphene. d) 2-probe *I–V* plot obtained for graphene-coated on SiO2 substrate.

characteristics indicative of the material's structural properties. The Raman spectra demonstrate that the synthesized graphene is not monolayer, as evidenced by the distinctive features observed in the spectra. Specifically, the presence of a shoulder peak in the G band (Figure 4b,e) and the 2D peak (Figure 4c,f) indicates the existence of defects, disorder, layer thickness variations, and strain effects within the graphene structure.[70–72] The G band, corresponding to the in-plane vibration of carbon atoms in a graphene lattice, exhibits a characteristic peak at ≈1580 cm^{-1}. The presence of a shoulder peak in the G band suggests the presence of structural defects or disorder within the graphene lattice, which may arise due to imperfections introduced during the microwave irradiation. Similarly, the 2D band ≈2650 cm^{-1}, associated with the second-order Raman scattering process and sensitive to the number of graphene layers and the presence of strain, typically appears as a single sharp peak in monolayer graphene. However, the observation of a broadened or asymmetric 2D peak, as seen in Figure 4c,f, indicates the presence of layer thickness variations and strain effects within the graphene structure. Symmetric 2D peak with R2 value above 0.98 confirms presence of monolayers or few layers of graphene in the synthesized sample (Figure S3, Supporting Information). While 2D peak >2700 cm^{-1} correspond to graphite, successful exfoliation will shift this peak toward lower frequency (2640–2680 cm^{-1}). 2D1 and D1+G peaks are often cited in literature.[73] Moreover, present defects such as vacancies/Stone-Wales, residual local straining (caused by severe thermal stress) and surface oxygen functionalities (due to ambient processing) can give rise to changes in 2D peak position. Since Raman spectroscopy is carried out on powder consisting of thousands of exfoliated sheets restacked together (not at equilibrium inter-layer distance as graphite, rather loosely bound) in the system, several sheets having different 2D peak positions are supposed to be present.[74–76]

XPS identified the chemical composition and oxidation state of the synthesized graphene. The XPS spectra in **Figure 5a** revealed prominent binding energy peaks corresponding to the C 1s and O 1s states at 284.7 and 523.2 eV, respectively. The detailed analysis of the C 1s peak, as presented in Figure 5b, further elucidates the chemical environment of the carbon atoms in the graphene lattice. This observation suggests that the graphene experienced slight oxidation during the microwave expansion process, resulting in the incorporation of oxygen-containing functional groups onto the graphene surface. The oxidation of graphene is a common phenomenon observed during synthesis processes involving exposure to high temperatures and oxidative environments. While the presence of oxygen-containing groups may introduce defects and alter the electronic properties of graphene, it can also enhance its dispersibility and compatibility with certain functionalization processes, thereby expanding its potential applications. UV-visible (UV-vis) spectroscopy was utilized to investigate the bandgap characteristics of the synthesized graphene. The UV–vis spectra in Figure 5c revealed a nearly straight absorption line in the wavelength range of 400–800 nm, indicative of lack of the bandgap of the synthesized graphene. This observation aligns with the expected electronic structure of graphene, which

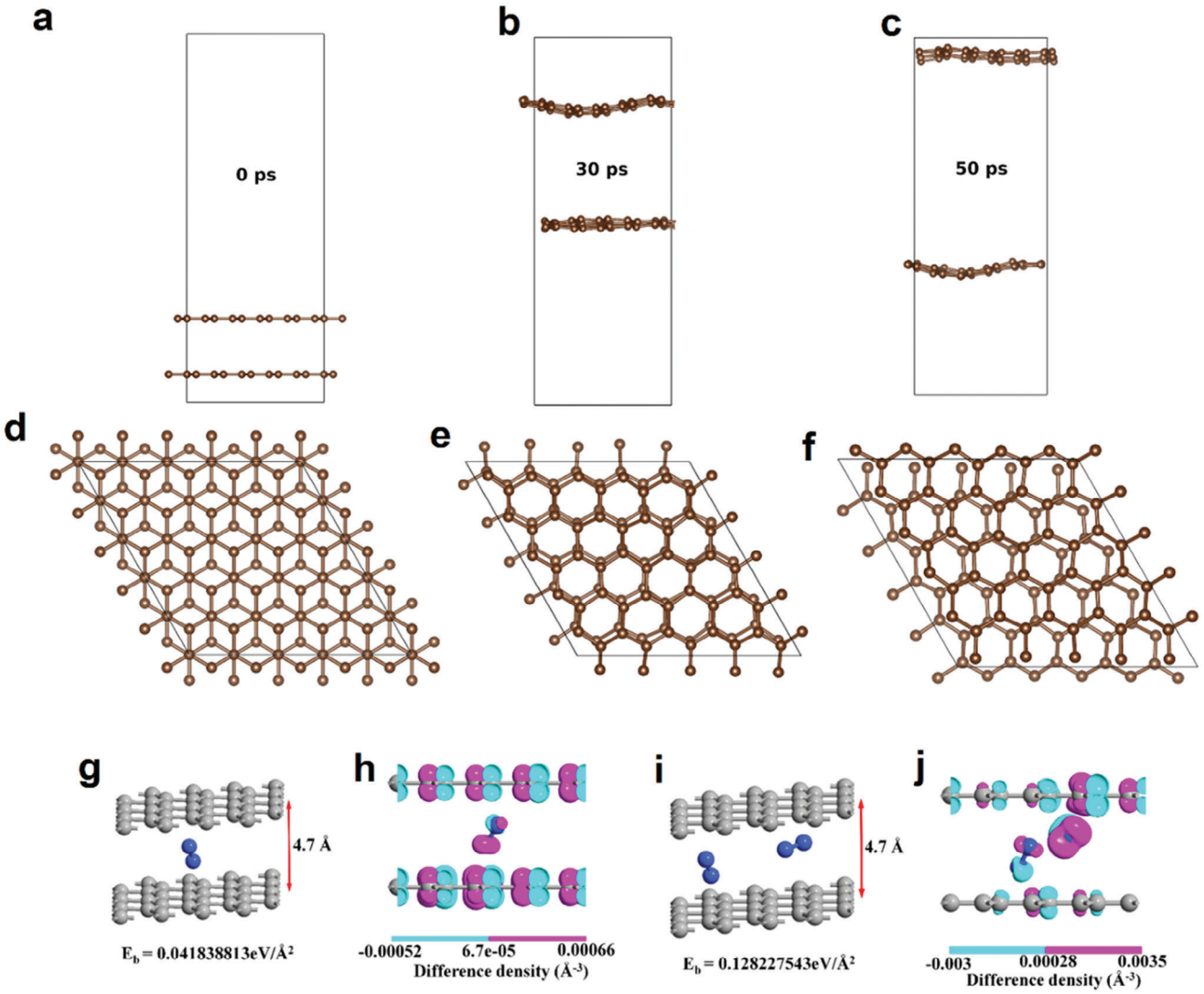

Figure 6. Molecular dynamics simulation for two layers of graphene under microwave expansion followed by cryoquenching for a,d) 0 ps, b,e) 30 ps, and c,f) 50 ps.DFT calculations for binding energies and charge density difference profiles of two layers of graphene with liquid nitrogen molecules intercalated between the layers for g,h) one molecule of N_2 and i,j) two molecules of N_2.

typically exhibits semi metallic behavior with a zero bandgap. The current-voltage (I/V) characteristic plot in Figure 5d of the synthesized graphene indicates its good conductivity. The linear relationship between current and voltage in the I/V plot suggests that the graphene exhibits ohmic behavior, with low resistance and good electrical conductivity.

To get better understanding of the microwave expansion process, Born Oppenheimer Molecular Dynamics was carried out on bilayer graphene. The system was brought from room temperature to microwave exposure condition (1200 K) and molecular dynamics simulation snapshots at 0, 30, and 50 ps undisputedly suggest enormous expansion of bilayers from 3.3 to 6.7 Å at 30 ps and 12.4 Å at 50 ps (**Figure** 6a–f). Even though microwave expansion of graphite at 1200 K where inter-layer distance increases to 12.4 Å, itself is very high; however, when microwave is switched OFF, it would contract upon cooling to room temperature (ambient condition). Once graphite is microwave expanded, then it would be easy for nitrogen molecules to intercalate in between the layers of graphite, if the expanded graphite is instantly exposed to liquid nitrogen. In expanded form itself, nitrogen molecule will chip in. In order to understand the liquid nitrogen intercalation effect during cryoquenching of the bilayer system (at 4.7 Å, mildly expanded configuration of graphite), DFT calculations were carried out, which suggested binding energy of + 0.042 and + 0.128 eV $Å^{-2}$ when one and two nitrogen molecules are intercalated between the graphene layers (Figure 6g–j). DFT results clearly indicate the severe instability of intercalated graphene system with liquid nitrogen embedded into it vis-a-vis without intercalation (Figure S4, Supporting Information).

The MECQ method offers several advantages, including low cost, high yield, rapid synthesis, facile operation, and the ability to produce graphene with large lateral dimensions and

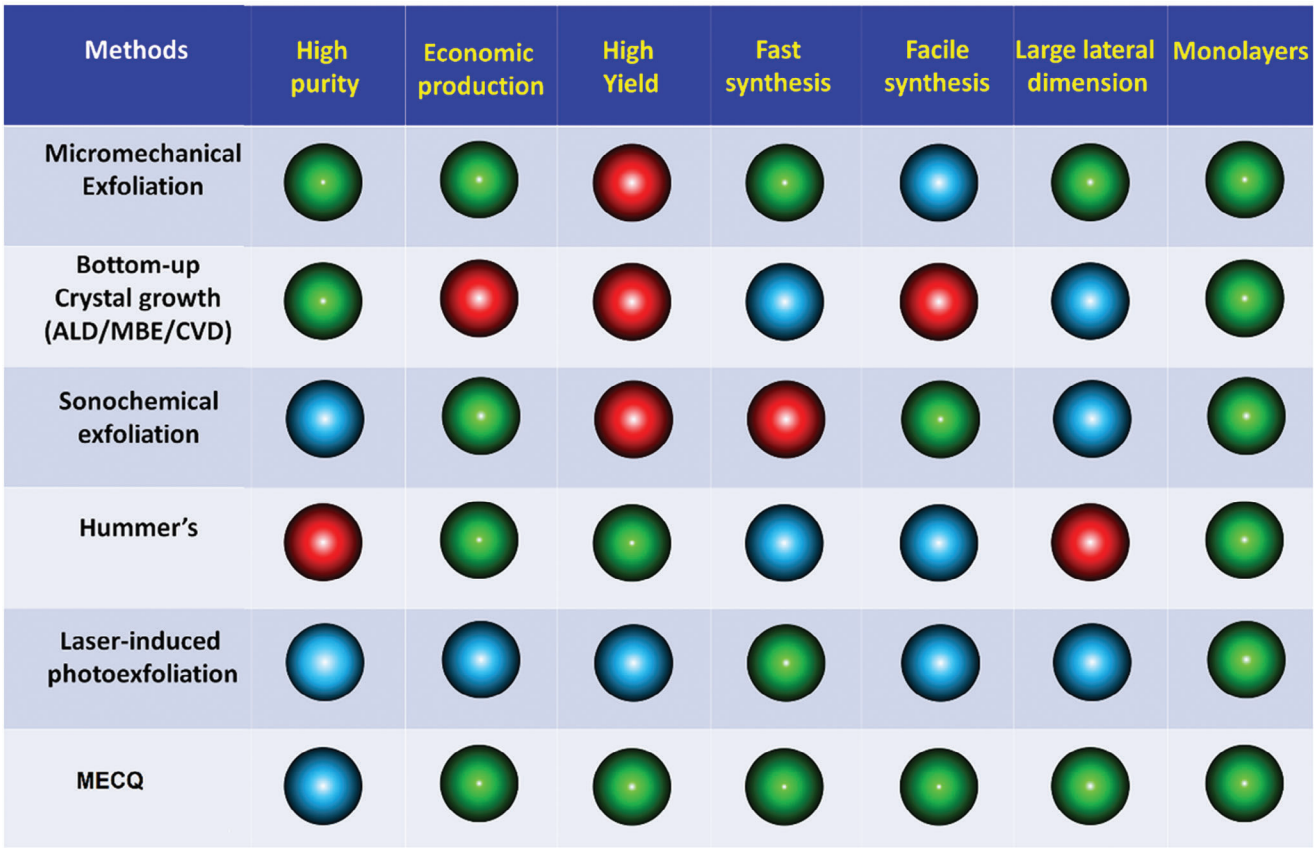

Figure 7. Comparative analysis of MECQ synthesis vis-à-vis various other contemporary methods of synthesis of graphene. Green means "**High**", red means "**Low**" and blue means "**moderate**".

monolayer structures compared to other existing graphene synthesis techniques, including micromechanical exfoliation, bottom-up crystal growth, sonochemical exfoliation, Hummer's method, and laser-induced photoexfoliation (**Figure 7**). However, it is noted that the selectivity of number of layers of the synthesized product may not as high as that for bottom-up crystal growth e.g. atomic layer deposition (ALD), molecular beam epitaxy (MBE), or chemical vapor deposition (CVD) etc. as it contains multi-layer graphene. This comparative analysis highlights the unique strengths and limitations of the MECQ method in relation to other established graphene synthesis approaches, providing valuable insights for researchers and practitioners in the field. Combinatorial MECQ approach does not involve any chemical reagents and thus provides a facile and environmental-friendly strategy to yield high-quality electronic grade graphene, which can be extended to other 2D materials as well.[77]

A BN/graphene heterolayered electrostatic mercury droplet switching device was fabricated. The device geometry is illustrated in **Figure** 8a. DRS spectrum in Figure 8b shows absorption in blue-cyan range with a mild hump at ≈300 nm, indicating the hybridization of orbitals of graphene and BN. Raman spectrum for the BN/graphene heterolayer in Figure 8c shows characteristic D, G, 2D bands or graphene at ≈1330, 1570, and 2660 cm^{-1} and BN characteristic peak at ≈1365 cm^{-1}. Slight shift ≈5 cm^{-1} in G peak in Raman spectrum as compared to pristine graphene also attests to hybridization of p_z-p_z orbitals in B-BN heterolayers. The electrowetting capability of the device with a mercury droplet was investigated (Figure 8d). Figure S5 (Supporting Information) suggests slight change in contact angle from 133° (at 0 V) to 130° (at 5 V). As observed, the mercury droplet exhibits a slight change in wettability from 0–15 V, and beyond 20 V, it begins to roll. At 30 V, there is a clear depiction of the displacement of the mercury droplet over the device (Figure 8e).

In general, the applied voltage on a droplet can alter its wettability on the contact surface. The contact angle decreases with an increase in the applied voltage, as described by the Young-Lippmann equation:

$$Cos\,\theta = Cos\,\theta_0 + \frac{1}{2\gamma}\left(\varepsilon_0\varepsilon_r\right)V^2 \quad (1)$$

We observed a decrement in the contact angle with a gradual increase in applied voltage up to 15 V. However, above 20 V, the mercury droplet started to roll. For a droplet to begin rolling, the electrowetting force $F_{electro}$ must overcome the contact angle hysteresis force F_h.

$$F_{electro} = \left(\delta\gamma_{LV}/\delta V\right)L \quad (2)$$

$$F_h = \gamma_{LV}\left(Cos\,\theta_r - Cos\,\theta_a\right)L \quad (3)$$

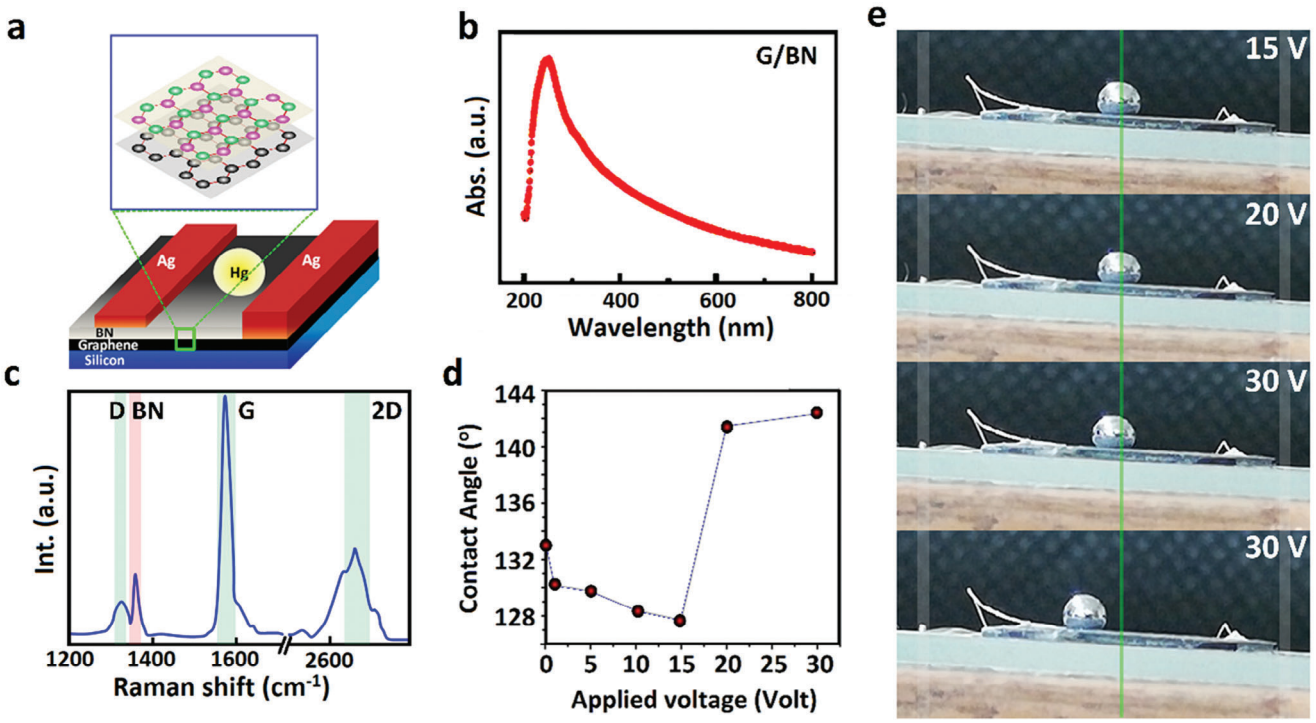

Figure 8. a) Schematic diagram of the BN/graphene heterolayer-based electrostatic droplet switch, b) DRS spectrum and c) Raman spectrum of BN/graphene heterolayer, d) Electrowetting plot (Contact angle variation with applied voltage) for BN/graphene heterolayer and e) demonstration of electrorolling of mercury droplet over BN/graphene heterolayers in electrostatic droplet switch device.

The rolling Voltage V_r where these forces balance, can be given by:

$$V_r^2 = \frac{\left[2\gamma_{LV}\ \left(Cos\,\theta_r - Cos\,\theta_a\right)\right]}{\varepsilon_0\varepsilon_r} \quad (4)$$

where γ_{LV} is the liquid-vapor surface tension, ε_0 is the permittivity of free space, and ε_r is the relative permittivity of the dielectric layer. With a higher effective relative permittivity of the BN/graphene interface, the rolling voltage is reduced, which is precisely what is needed for electrostatic droplet switching device applications.

Graphene maintains high performance and reliability on suitable substrates, even after extensive use.[24] Bolotin et al.[78] highlighted the high electron mobility and stability of graphene, even under conditions of repeated electrical cycling. Additionally, Yazyev and Louie[79] discussed the robust electronic transport properties of polycrystalline graphene, further supporting its durability in electronic applications. Graphene synthesized by MECQ in the present report, possessed atomic flatness. Moreover, defect-free and surface functionality-free nature of obtained graphene results in poor wetting by mercury fluid giving rise to higher contact angles >120°, necessary for rolling on the surface. High electronic mobility of defect free graphene (which is often deemed as one of the most suitable candidates for low power electronics) will be apt for low power electrostatic droplet switching. Metallic fluid-based (mercury droplet) switching, especially on atom-flat graphene sheets exhibits excellent cyclic performance with applied voltage.[80]

3. Conclusion

The strategic exploitation of exotic thermodynamic conditions caused by microwave irradiation, coupled with cryoquenching, presents a unique avenue for synthesizing 2D materials in effortless (facile) manner with enhanced efficiency and scalability. This novel approach capitalizes on the inherent response of van der Waals crystals to extreme thermal stress, leading to rapid and controlled exfoliation. One can tune microwave power (800 and 640 W used in separate synthesis experiments) to tailor the quality of the synthesized graphene. The microscopic (SEM, AFM, TEM) and spectroscopic (Raman, XPS) analyses collectively affirm the successful synthesis of graphene through this innovative approach. MD simulation and DFT calculations reveal intricate details of microwave expansion and cryoquenching process. Electrostatic droplet switching has been successfully demonstrated for a mercury droplet on a BN/graphene heterolayered device, with electrorolling observed at voltages >20 V.

This groundbreaking research not only expands the arsenal of synthetic methodologies for 2D materials but also introduces a paradigm shift in the utilization of thermal stress for exfoliation. The implications of this work extend beyond graphene synthesis, offering a pathway for the scalable production of various 2D materials with very high chemical phase purity. The economic and scalable nature of this approach holds the potential to accelerate the integration of 2D materials into diverse technological applications, paving the way for transformative advancements in the field.

4. Experimental Section

Synthesis of Graphene: Graphene was synthesized using the Microwave Expansion Cryoquenching (MECQ) method, employing graphite powder (Sigma–Aldrich, 99.99 %) as the precursor material. The synthesis process involved the following steps: a) Graphite powder was subjected to microwave exposure in a convection microwave oven (IFB 25BC3 25 Litres) and its expansion was attained within a duration of 10 min by using different power levels (640 and 800 W) in two different experiments, b) Following microwave expansion, the sample was rapidly quenched with liquid nitrogen by pouring the fluid and allowing it to remain for 5 min. c) Subsequently, the sample were undergone through ultrasonication (Cole Parmer, 40 KHz) for 90 min in IPA (Sigma–Aldrich) to ensure proper exfoliation. d) The supernatant, comprising the top 1/3rd of the synthesized dispersion, was collected and centrifuged (Remi, R-24) at 3000 rpm for 5 min.

Characterization: The collected supernatant was transferred onto silicon substrates and dried at 80 °C for 1 h to prepare the samples for characterization. The synthesized graphene samples were characterized using microscopy techniques such as SEM (Hitachi S-4800), AFM (Agilent Model No.5500) to assess their structural and morphological properties as well as various spectroscopic techniques such as UV–vis spectroscopy (Perkin Elmer Lambda-35), Raman spectroscopy (Seki Technotron Corporation, Japan) having 633 nm He-Ne laser and XPS (ESCA+ Omicron Nano Technology GmbH) to quantitatively characterize chemical phase purity. TEM Analysis: Additionally, the supernatant was directly transferred onto TEM grids and dried for further characterization using TEM (JEOL JEM 2100). I/V measurements were carried out with graphene sheets transferred on lithographically fabricated titanium/gold electrodes and the current was monitored employing Kiethley 2420 source meter.

Density Functional Theory (DFT): The present study employed first-principal-based density functional theory (DFT) calculations. The self-consistent calculation was done using the Perdew–Burke–Ernzerhof (PBE) exchange-correlation functional under the generalized gradient approximation (GGA). The study adopted the double ζ basis set, implemented in the Atomistix Toolkit package (ATK). A $9 \times 9 \times 1$ Monkhorst–Pack scheme k-point grid was used in the first Brillouin zone with the maximum residual force is <0.01 eVÅ^{-1}. The density mesh cutoff is 75 Hartree. In all of the supercell models, a vacuum thickness >15 Å along the z direction was employed to avoid interaction between the top and bottom surfaces of the adjacent slabs. Binding energy of graphene bilayer intercalated with liquid nitrogen molecules were calculated by using the following formula.

$$\textit{Binding energy } (E_b) = \textit{Total energy of system} - mN_2 - \textit{Bilayer of graphene/surface area} \quad (5)$$

Born Oppenheimer Molecular Dynamics: To consider the exfoliation process in higher temperature, we have performed constant-temperature BOMD simulations considering the canonical ensemble (NVT) as implemented in the Vienna Ab initio Simulation Package (VASP).[81–83] A 5X5 bilayer graphene supercell for BOMD calculations was used with an increased c lattice parameter (30 Angstrom). A Nose–Hoover thermostat was used to adjust the temperature at 1200 K during the simulations, and a time step of 1 fs was considered to integrate the equation of motion.[84,85] The study ran the simulation up to 50 ps to observe the exfoliation process.

Electrostatic Droplet Switch Fabrication: Silicon substrate was thoroughly cleaned and first graphene (utilizing graphene synthesized and reported in the present article) layer was coated onto it employing spin coating and heating layer-by-layer with each drop of dispersion and thus constituting a continuous graphene layer over the substrate. Part of the graphene surface was kept masked with teflon tape and coated with BN layer by spin coating. After BN coating was finished, teflon tape was taken off and silver electrodes (one electrode on bare graphene part and another on BN coating) were fabricated. A clean device was obtained by nitrogen blowing and adequate drying (≈80 °C, 20 min). Standard constant DC voltage source Kiethley 2420 source meter was used for applying bias to the switching device.

Supporting Information

Supporting Information is available from the Wiley Online Library or from the author.

Acknowledgements

The authors acknowledge the Indian Institute of Technology Patna for experimental facilities. P.K. acknowledges the Department of Science and Technology, Govt. of India, for a Research grant under the Ramanujan Fellowship (Sanction No. SB/S2/RJN-205/2014).

Open access publishing facilitated by The University of Newcastle, as part of the Wiley - The University of Newcastle agreement via the Council of Australian University Librarians.

Conflict of Interest

The authors declare no conflict of interest.

Author Contributions

S.C., T.S., and Z.L. contributed equally to this work. P.K. conceived the idea. T.S., E.K., and S.C., carried out MECQ synthesis of graphene. Z.L. analyzed the results. R.S. carried out electrowetting experiment. A.B. carried out M.D. simulation. Puja carried out DFT calculation under supervision of S.J.R. A.V. was consulted for material purity analysis. P.K. and Z.L. wrote the manuscript. The project was carried out in overall supervision by PK.

Data Availability Statement

The data that support the findings of this study are available in the supplementary material of this article.

Keywords

cryoexfoliation, electrostatic droplet switching, graphene, microwave

Received: May 29, 2024
Revised: June 13, 2024
Published online: July 3, 2024

[1] K. S. Novoselov, A. K. Geim, S. V. Morozov, D. Jiang, Y. Zhang, S. V. Dubonos, I. V. Grigorieva, A. A. Firsov, *Science* **2004**, *306*, 666.
[2] K. S. Novoselov, A. K. Geim, S. V. Morozov, D. Jiang, M. I. Katsnelson, I. V. Grigorieva, S. V. Dubonos, A. A. Firsov, *Nature* **2005**, *438*, 197.
[3] P. Ranjan, S. Gaur, H. Yadav, A. B. Urgunde, V. Singh, A. Patel, K. Vishwakarma, D. Kalirawana, R. Gupta, P. Kumar, *Nano Convergence* **2022**, *9*, 26.
[4] L. Li, J. Kim, C. Jin, G. J. Ye, D. Y. Qiu, F. H. da Jornada, Z. Shi, L. Chen, Z. Zhang, F. Yang, K. Watanabe, T. Taniguchi, W. Ren, S. G. Louie, X. H. Chen, Y. Zhang, F. Wang, *Nat. Nanotechnol.* **2017**, *12*, 21.
[5] S. Chahal, R. Bhushan, P. Kumari, X. Guan, J. M. Lee, S. J. Ray, A. K. Thakur, A. Vinu, P. Kumar, *Matter* **2024**, *7*, 237.
[6] A. J. Mannix, X.-F. Zhou, B. Kiraly, J. D. Wood, D. Alducin, B. D. Myers, X. Liu, B. L. Fisher, U. Santiago, J. R. Guest, M. J. Yacaman, A. Ponce, A. R. Oganov, M. C. Hersam, N. P. Guisinger, *Science* **2015**, *350*, 1513.
[7] P. Ranjan, T. K. Sahu, R. Bhushan, S. S. Yamijala, D. J. Late, P. Kumar, A. Vinu, *Adv. Mater.* **2019**, *31*, 1900353.

[8] P. Ranjan, J. M. Lee, P. Kumar, A. Vinu, *Adv. Mater.* **2020**, *32*, 2000531.
[9] S. Chahal, P. Ranjan, M. Motlag, S. S. R. K. C. Yamijala, D. J. Late, E. H. S. Sadki, G. J. Cheng, P. Kumar, *Adv. Mater.* **2021**, *33*, 2102039.
[10] K. Vishwakarma, S. Rani, S. Chahal, C.-Y. Lu, S. J. Ray, C.-S. Yang, P. Kumar, *Phys. Chem. Chem. Phys.* **2022**, *24*, 12816.
[11] X. Guan, P. Kumar, Z. Li, T. K. A. Tran, S. Chahal, Z. Lei, C.-Y. Huang, C.-H. Lin, J.-K. Huang, L. Hu, Y.-C. Chang, L. Wang, J. S. J. Britto, L. Panneerselvan, D. Chu, T. Wu, A. Karakoti, J. Yi, A. Vinu, *Adv. Sci.* **2023**, *10*, 2205809.
[12] Z. li, X. Guan, G. Pandey, S. Chahal, A. Bandyopadhyay, K. Awasthi, P. Kumar, A. Vinu, *Small* **2024**, https://doi.org/10.1002/smll.202307610.
[13] P. Vogt, P. De Padova, C. Quaresima, J. Avila, E. Frantzeskakis, M. C. Asensio, A. Resta, B. Ealet, G. Le Lay, *Phys. Rev. Lett.* **2012**, *108*, 155501.
[14] M. E. Dávila, L. Xian, S. Cahangirov, A. Rubio, G. Le Lay, *New J. Phys.* **2014**, *16*, 095002.
[15] S. Chahal, A. Bandyopadhyay, S. P. Dash, P. Kumar, *J. Phys. Chem. Lett.* **2022**, *13*, 6487.
[16] S. Chahal, A. Bandyopadhyay, C.-S. Yang, P. Kumar, *npj 2D Mater. Appl.* **2023**, *7*, 55.
[17] T. K. Sahu, N. Kumar, S. Chahal, R. Jana, S. Paul, M. Mukherjee, A. H. Tavabi, A. Datta, R. E. Dunin-Borkowski, I. Valov, A. Nayak, P. Kumar, *Nat. Nanotechnol.* **2023**, *18*, 1430.
[18] S. Chahal, S. M. Kauzlarich, P. Kumar, *ACS Mater. Lett.* **2021**, *3*, 631.
[19] P. Kumar, J. Liu, P. Ranjan, Y. Hu, S. S. Yamijala, S. K. Pati, J. Irudayaraj, G. J. Cheng, *Small* **2018**, *14*, 1703346.
[20] S. Chahal, T. K. SahuChahal, S. Kar, H. Ranjan, S. J. Ray, P. Kumar, *Eng. Rep.* **2024**, *6*, e12787.
[21] T. K. Sahu, S. P. Sahu, K. P. S. S. Hembram, J.-K. Lee, V. Biju, P. Kumar, *NPG Asia Mater.* **2023**, *15*, 49.
[22] M. Naguib, M. Kurtoglu, V. Presser, J. Lu, J. Niu, M. Heon, L. Hultman, Y. Gogotsi, M. W. Barsoum, *Adv. Mater.* **2011**, *23*, 4248.
[23] C. N. R. Rao, K. S. Subrahmanyam, H. S. S. Ramakrishna Matte, B. Abdulhakeem, A. Govindaraj, B. Das, P. Kumar, A. Ghosh, D. J. Late, *Sci. Technol. Adv. Mater.* **2010**, *11*, 054502.
[24] C. R. Dean, A. F. Young, I. Meric, C. Lee, L. Wang, S. Sorgenfrei, K. Watanabe, T. Taniguchi, P. Kim, K. L. Shepard, J. Hone, *Nat. Nanotechnol.* **2010**, *5*, 722.
[25] F. Bonaccorso, Z. Sun, T. Hasan, A. C. Ferrari, *Nat. Photonics* **2010**, *4*, 611.
[26] P. Kumar, L. S. Panchakarla, S. Venkataprasad Bhat, U. Maitra, K. S. Subrahmanyam, C. N. R. Rao, *Nanotechnology* **2010**, *21*, 385701.
[27] I. Khan, A. A. M. Ibrahim, M. Sohail, A. Qurashi, *Ultrasonics Sonochem.* **2017**, *37*, 669.
[28] W. Han, R. K. Kawakami, M. Gmitra, J. Fabian, *Nat. Nanotechnol.* **2014**, *9*, 794.
[29] S. R. Das, Q. Nian, M. Saei, S. Jin, D. Back, P. Kumar, D. B. Janes, M. A. Alam, G. J. Cheng, *ACS Nano* **2015**, *9*, 11121.
[30] Y. Hu, S. Lee, P. Kumar, Q. Nian, W. Wang, J. Irudayaraj, G. J. Cheng, *Nanoscale* **2015**, *7*, 19885.
[31] S. Lee, P. Kumar, Y. Hu, G. J. Cheng, J. Irudayaraj, *Chem. Commun.* **2015**, *51*, 15494.
[32] J. Liu, P. Kumar, Y. Hu, G. J. Cheng, J. Irudayaraj, *J. Phys. Chem. C* **2015**, *119*, 6331.
[33] J. Liu, Y. Hu, P. Kumar, X. Liu, J. M. K. Irudayaraj, G. J. Cheng, *Adv. Opt. Mater.* **2021**, *9*, 2001830.
[34] Y. Hu, P. Kumar, Y. Xuan, B. Deng, M. Qi, G. J. Cheng, *Adv. Opt. Mater.* **2016**, *4*, 1811.
[35] R. Bhushan, P. Kumar, A. K. Thakur, *Solid State Ionics* **2020**, *353*, 115371.
[36] H. Ranjan, P. Ranjan, T. K. Sahu, R. K. Sharma, P. Kumar, *J. Mater. Res.* **2023**, *38*, 1792.
[37] K. S. Subrahmanyam, P. Kumar, U. Maitra, A. Govindaraj, K. P. S. S. Hembram, U. V. Waghmare, C. N. R. Rao, *Proc. Natl. Acad. Sci. USA* **2011**, *108*, 2674.
[38] K. Gopalakrishnan, K. S. Subrahmanyam, P. Kumar, A. Govindaraj, C. N. R. Rao, *RSC Adv.* **2012**, *2*, 1605.
[39] M. Motlag, P. Kumar, K. Y. Hu, S. Jin, J. Li, J. Shao, X. Yi, Y.-H. Lin, J. C. Walrath, L. Tong, X. Huang, R. S. Goldman, L. Ye, G. J. Cheng, *Adv. Mater.* **2019**, *31*, 1900597.
[40] S. Chahal, A. K. Nair, S. J. Ray, J. Yi, A. Vinu, P. Kumar, *Chem. Eng. J.* **2022**, *450*, 138447.
[41] T. K. Sahu, M. Motlag, A. Bandyopadhyay, N. Kumar, G. J. Cheng, P. Kumar, *Adv. Sci.* **2022**, *9*, 2202695.
[42] P. Kumar, J. Liu, M. Motlag, L. Tong, Y. Hu, X. Huang, A. Bandopadhyay, S. K. Pati, L. Ye, J. Irudayaraj, G. J. Cheng, *Nano Lett.* **2019**, *19*, 283.
[43] S. Bae, H. Kim, Y. Lee, X. Xu, J.-S. Park, Y. Zheng, J. Balakrishnan, T. Lei, H. Ri Kim, Y. I. Song, Y.-J. Kim, K. S. Kim, B. Özyilmaz, J.-H. Ahn, B. H. Hong, S. Iijima, *Nat. Nanotechnol.* **2010**, *5*, 574.
[44] K. S. Subrahmanyam, L. S. Panchakarla, A. Govindaraj, C. N. R. Rao, *J. Phys. Chem. C* **2009**, *113*, 4257.
[45] S. Park, R. S. Ruoff, *Nat. Nanotechnol.* **2009**, *4*, 217.
[46] Y. Hernandez, V. Nicolosi, M. Lotya, F. M. Blighe, Z. Sun, S. De, I. T. McGovern, B. Holland, M. Byrne, Y. K. Gun'Ko, J. J. Boland, P. Niraj, G. Duesberg, S. Krishnamurthy, R. Goodhue, J. Hutchison, V. Scardaci, A. C. Ferrari, J. N. Coleman, *Nat. Nanotechnol.* **2008**, *3*, 563.
[47] P. Kumar, *RSC Adv.* **2013**, *3*, 11987.
[48] P. Kumar, A. Dey, J. Roques, L. Assaud, S. Franger, P. Parida, V. Biju, *ACS Materials Letters* **2022**, *4*, 263.
[49] D. V. Kosynkin, A. L. Higginbotham, A. Sinitskii, J. R. Lomeda, A. Dimiev, B. K. Price, J. M. Tour, *Nature* **2009**, *458*, 872.
[50] P. Kumar, L. S. Panchakarla, C. N. R. Rao, *Nanoscale* **2011**, *3*, 2127.
[51] P. Kumar, S. S. R. K. C. Yamijala, S. K. Pati, *J. Phys. Chem. C* **2016**, *120*, 16985.
[52] Y. Wang, Y. Liu, J. Zhang, J. Wu, H. Xu, X. Wen, X. Zhang, C. S. Tiwary, W. Yang, R. Vajtai, Y. Zhang, N. Chopra, I. N. Odeh, Y. Wu, P. M. Ajayan, *Sci. Adv.* **2017**, *3*, e1701500.
[53] J. Zhang, T. Zhu, Y. Wang, J. Cui, J. Sun, J. Yan, Y. Qin, X. Shu, Y. Zhang, J. Wu, C. S. Tiwary, P. M. Ajayan, Y. Wu, *Mater. Today* **2020**, *36*, 83.
[54] T. Zheng, M. Li, S. Zhou, Y. Zhao, Z. Zhong, C. Chen, *Journal of Porous Materials* **2022**, *29*, 331.
[55] J. Ouyang, L. Zhang, L. Li, W. Chen, Z. Tang, X. Ji, C. Feng, N. Tao, N. Kong, T. Chen, Y.-N. Liu, W. Tao, *Nano-Micro Lett.* **2021**, *13*, 90.
[56] L. Fan, D. Huang, Y. Wang, Z. Miao, Y. Ma, Q. Zhao, Z. Zha, *Chem. Commun.* **2019**, *55*, 2805.
[57] R. Quirós-Ovies, M. Laborda, N. M. Sabanés, L. Martín-Pérez, S. M.-D. Silva, E. Burzurí, V. Sebastian, E. M. Pérez, J. Santamaría, *ACS Nano* **2023**, *17*, 5984.
[58] J. Lin, Y. Huang, S. Wang, G. Chen, *Ind. Eng. Chem. Res.* **2017**, *56*, 9341.
[59] Y. Zhu, S. Murali, M. D. Stoller, A. Velamakanni, R. D. Piner, R. S. Ruoff, *Carbon* **2010**, *48*, 2118.
[60] H. Wang, W. Lv, J. Shi, H. Wang, D. Wang, L. Jin, J. Chao, P. A. van Aken, R. Chen, W. Huang, *ACS Sustainable Chem. Eng.* **2020**, *8*, 84.
[61] X. Zhu, J. Yang, X. She, Y. Song, J. Qian, Y. Wang, H. Xu, H. Li, Q. Yan, *J. Mater. Chem. A* **2019**, *7*, 5209.
[62] K. E. Petersen, *Proceedings of the IEEE* **1982**, *70*, 420.
[63] J. Kim, W. Shen, L. Latorre, C.-J. Kim, *Sens. Actuators, A* **2002**, *97–98*, 672.
[64] J. Kim, W. Shen, L. Latorre, C.-J. C. Kim, In *A Micromechanical Switch with Electrostatically Driven Liquid-Metal Droplet*, (Ed. E. Obermeier), Springer, Berlin, Heidelberg **2001**, pp. 748, https://doi.org/10.1007/97-8-364-25949-77178.
[65] S. Wenjiang, R. T. Edwards, K. Chang-Jin, *J. Microelectromech. Syst.* **2006**, *15*, 879.

[66] R. Bessler, U. Duerig, E. Koren, *Nanoscale Advances* **2019**, *1*, 1702.
[67] A. Laturia, M. L. Van de Put, W. G. Vandenberghe, *npj 2D Materials and Applications* **2018**, *2*, 6.
[68] J. E. Zorzi, C. A. Perottoni, *Comput. Mater. Sci.* **2021**, *199*, 110719.
[69] T. Kim, J. Lee, K.-H. Lee, *Carbon Lett.* **2014**, *15*, 15.
[70] A. Gupta, G. Chen, P. Joshi, S. Tadigadapa, *Nano Lett.* **2006**, *6*, 2667.
[71] L. G. Cançado, A. Jorio, E. H. M. Ferreira, F. Stavale, C. A. Achete, R. B. Capaz, M. V. O. Moutinho, A. Lombardo, T. S. Kulmala, A. C. Ferrari, *Nano Lett.* **2011**, *11*, 3190.
[72] A. C. Ferrari, D. M. Basko, *Nat. Nanotechnol.* **2013**, *8*, 235.
[73] S. P. Rosoiu, A. G. Pantazi, A. Petica, A. Cojocaru, S. Costovici, C. Zanella, T. Visan, L. Anicai, M. Enachescu, *Metals* **2020**, *10*, 1455.
[74] O. Frank, M. Mohr, J. Maultzsch, C. Thomsen, I. Riaz, R. Jalil, K. S. Novoselov, G. Tsoukleri, J. Parthenios, K. Papagelis, L. Kavan, C. Galiotis, *ACS Nano* **2011**, *5*, 2231.
[75] X. Wang, J. W. Christopher, A. K. Swan, *Sci. Rep.* **2017**, *7*, 13539.
[76] X. Gao, H. Sun, D.-H. Kang, C. Wang, Q. J. Wang, D. Nam, *Sci. Rep.* **2021**, *11*, 21402.
[77] Z. Ma, Z. Liu, Z. Cheng, *Chin. Chem. Lett.* **2020**, *31*, 1936.
[78] K. I. Bolotin, K. J. Sikes, Z. Jiang, M. Klima, G. Fudenberg, J. Hone, P. Kim, H. L. Stormer, *Solid State Commun.* **2008**, *146*, 351.
[79] O. V. Yazyev, S. G. Louie, *Nat. Mater.* **2010**, *9*, 806.
[80] R. Tabassian, J.-H. Oh, S. Kim, D. Kim, S. Ryu, S.-M. Cho, N. Koratkar, I.-K. Oh, *Nat. Commun.* **2016**, *7*, 13345.
[81] G. Kresse, J. Hafner, *Phys. Rev. B* **1993**, *47*, 558.
[82] G. Kresse, J. Furthmüller, *Comput. Mater. Sci.* **1996**, *6*, 15.
[83] G. Kresse, J. Furthmüller, *Phys. Rev. B* **1996**, *54*, 11169.
[84] S. Nosé, *J. Chem. Phys.* **1984**, *81*, 511.
[85] W. G. Hoover, *Phys. Rev. A* **1985**, *31*, 1695.